

Large-scale mass distribution in the Illustris simulation

M. Haider^{1*}, D. Steinhauser¹, M. Vogelsberger², S. Genel^{3†}, V. Springel^{4,5}
P. Torrey^{2,6} and L. Hernquist⁷

¹*Institut für Astro- und Teilchenphysik, Universität Innsbruck, Technikerstraße 25/8, A-6020 Innsbruck, Austria*

²*Kavli Institute for Astrophysics and Space Research, Massachusetts Institute of Technology, Cambridge, MA 02139, USA*

³*Department of Astronomy, Columbia University, 550 West 120th Street, New York, NY 10027, USA*

⁴*Heidelberg Institute for Theoretical Studies, Schloss-Wolfsbrunnengasse 35, D-69118 Heidelberg, Germany*

⁵*Zentrum für Astronomie der Universität Heidelberg, Astronomisches Recheninstitut, Mönchhofstr. 12-14, D-69120 Heidelberg, Germany*

⁶*TAPIR, California Institute of Technology, Mailcode 350-17, Pasadena, CA 91125, USA*

⁷*Harvard-Smithsonian Center for Astrophysics, 60 Garden Street, Cambridge, MA 02138, USA*

Accepted 2016 January 8. Received 2015 December 21; in original form 2015 August 6

ABSTRACT

Observations at low redshifts thus far fail to account for all of the baryons expected in the Universe according to cosmological constraints. A large fraction of the baryons presumably resides in a thin and warm-hot medium between the galaxies, where they are difficult to observe due to their low densities and high temperatures. Cosmological simulations of structure formation can be used to verify this picture and provide quantitative predictions for the distribution of mass in different large-scale structure components. Here we study the distribution of baryons and dark matter at different epochs using data from the Illustris simulation. We identify regions of different dark matter density with the primary constituents of large-scale structure, allowing us to measure mass and volume of haloes, filaments and voids. At redshift zero, we find that 49 % of the dark matter and 23 % of the baryons are within haloes more massive than the resolution limit of $2 \times 10^8 M_{\odot}$. The filaments of the cosmic web host a further 45 % of the dark matter and 46 % of the baryons. The remaining 31 % of the baryons reside in voids. The majority of these baryons have been transported there through active galactic nuclei feedback. We note that the feedback model of Illustris is too strong for heavy haloes, therefore it is likely that we are overestimating this amount. Categorizing the baryons according to their density and temperature, we find that 17.8 % of them are in a condensed state, 21.6 % are present as cold, diffuse gas, and 53.9 % are found in the state of a warm-hot intergalactic medium.

Key words: galaxies: haloes – cosmology: dark matter – large-scale structure of Universe.

1 INTRODUCTION

The large-scale structure of the Universe is determined by the dominant dark matter, which makes up 26 % of today’s mass–energy content of the Universe. As dark matter is not detectable directly, the large-scale structure must be inferred from the baryons. Recent analysis (Planck Collaboration 2015) of the cosmic microwave background fluctuations by the *Planck* mission found that baryons amount to $\Omega_b = 4.8$ % of the present-day critical density of the Universe. This corresponds to a mean baryon density of $\rho_b = 4.1 \times 10^{-31} \text{g cm}^{-3}$. An independent measurement of the baryon content of the Universe is possible through the

theory of big bang nucleosynthesis, as it allows one to infer the baryon content from the abundance ratio of light elements. The measurements of the abundance ratio of deuterium to hydrogen (D/H) (Kirkman et al. 2003) are in very good agreement with the baryon content derived from the cosmic microwave background fluctuations. At higher redshifts, the baryons were not fully ionized. This allows their detection in denser regions through HI absorption lines in the spectrum of background quasars, the so-called Lyman alpha (Ly α) forest. The amount of gas needed to produce the observed absorption lines in the Ly α forest is in good agreement with the cosmic baryon fraction Ω_b (Weinberg et al. 1997).

At low redshifts, however, observations fail to account for all the baryons detected at higher redshifts (Fukugita & Peebles 2004; Bregman 2007). While X-ray observations of

* E-mail: markus.haider@uibk.ac.at

† Hubble fellow

galaxy clusters do find baryon contents close to the primordial value (Simionescu et al. 2011), and OVII absorption line measurements at X-ray energies hint at large reservoirs of hot gas around spiral galaxies (Gupta et al. 2012), approximately 30 % of the baryons are still not accounted for in the local Universe (Shull et al. 2012). The baryons are not only missing on cosmological scales, but the baryon-to-dark matter ratio in galaxies also falls short of the primordial ratio (Bell et al. 2003; McGaugh et al. 2010).

Based on hydrodynamical simulations (Davé et al. 2001), we expect that a significant amount of the baryons are hidden in the state of a thin warm-hot intergalactic medium (WHIM) with temperatures between 10^5 and 10^7 K. Through HI and OVI surveys (Danforth & Shull 2008), it is possible to probe the colder parts of the low-redshift intergalactic medium. However, the gas is too diffuse and the temperatures are insufficient to be detectable with the current generation of X-ray satellites (Kaastra et al. 2013), except in the densest regions between galaxy clusters (Nicasastro et al. 2005, 2013). The question of how the baryons are distributed and whether they follow the filaments of the cosmic web is not well constrained observationally, and consequently, cosmological simulations of structure formation are important tools for making predictions about the large-scale distribution of baryons (Cen & Ostriker 1999, 2006; Davé et al. 1999, 2001; Smith et al. 2010). In this paper, we investigate the distribution of baryons and dark matter using data from the Illustris simulation (Vogelsberger et al. 2014b). In Section 2, we give a short overview of the simulation and discuss the methods we used. Our results are presented in Section 3. Specifically, in 3.1, we investigate the amount of matter inside haloes and compute the baryon fraction for haloes of different masses. In Section 3.2, we examine the distribution of matter with respect to the dark matter density. This allows us to decompose the simulation volume into haloes, filaments and voids, and measure the mass, volume and redshift evolution of these components. In Section 3.3, we look at the distribution of the baryons in the temperature–density space and compute the mass fraction and redshift evolution of the condensed, diffuse, hot and WHIM phases. We discuss the results in Section 4 and close with a summary in Section 5.

2 SIMULATION & METHODS

We analyse data from the Illustris simulation, which is a cosmological hydrodynamics simulation of galaxy formation in a $(106.5 \text{ Mpc})^3$ volume [corresponding to a $(75 \text{ Mpc/h})^3$ periodic box]. The gas and dark matter were evolved using the AREPO moving-mesh code (Springel 2010). In addition to gravity and hydrodynamics, the simulation includes sub-grid models for star formation, active galactic nuclei (AGN) feedback and gas cooling [see Vogelsberger et al. (2013) and Torrey et al. (2014) for details on the implemented feedback models and the parameter selection]. Dark matter and gas are represented by 1820^3 resolution elements each, resulting in an initial mass resolution of $1.26 \times 10^6 M_\odot$ for gas and $6.26 \times 10^6 M_\odot$ for dark matter. The simulation uses a standard Λ CDM model with $H = 70.4$, $\Omega_0 = 0.2726$, $\Omega_\Lambda = 0.7274$ and $\Omega_b = 0.0456$. It was started at redshift $z = 127$ and evolved all the way to the present epoch. The

Illustris simulation produced a galaxy mass function and a star formation history which are in reasonably good agreement with observations. Remarkably, it also yielded a realistic morphological mix of galaxies. An overview of basic results is given in Vogelsberger et al. (2014b), Vogelsberger et al. (2014a) and Genel et al. (2014), and recently, all of the simulation data has been made publicly available (Nelson et al. 2015).

In Section 3.1, we use the halo catalogue of the Illustris simulation, which has been generated using the SUBFIND halo-finding algorithm (Springel et al. 2001). SUBFIND searches for gravitationally bound overdensities and computes the dark matter, gas and stellar mass which is bound to a halo or subhalo. In the subsequent analysis, we compute the density fields of gas, stars, baryonic matter and dark matter on a uniform grid with 1024^3 cells. To this end, the dark matter and gas particles are mapped conservatively to the grid using a smoothed particle hydrodynamics (SPH) kernel technique. For the dark matter, we set the smoothing length to be the radius of a sphere containing the 64 nearest dark matter particles, as is done also in SUBFIND. The gas cells are mapped using three times $r_c = (3V_{\text{cell}}/4\pi)^{1/3}$, where V_{cell} is the volume of a Voronoi cell. The stellar and black hole particles have been mapped using the particle in cell method with a nearest grid point assignment, as they are not tracers of an extended density field. We should note that the densities given in this analysis are thus average densities over the volume of individual cells, which are 104 kpc on a side.

The baryon densities and temperatures used in Section 3.3 have been computed directly from the Voronoi cells of the simulation and do not involve any additional smoothing. For comparison, we also use a variant of the Illustris simulation where cooling, star formation and feedback have been switched off. This simulation, which we will refer to as non-radiative run, has only half the resolution of the full physics simulation.

3 RESULTS

In Section 3.1, we investigate the mass fraction of baryons and dark matter in haloes and compute the baryon-to-halo mass ratio. In Section 3.2, we examine the mass distribution with respect to the dark matter density. With the help of cuts in dark matter density, we divide the simulation volume into haloes, filaments and voids. In Section 3.3, we analyse the baryon distribution in temperature–density space.

3.1 Mass in haloes

In Table 1, we give the mass fraction of dark matter and baryons residing inside the identified SUBFIND haloes. The mass fractions are calculated using the mass of all particles which are gravitationally bound to haloes. Only main haloes were considered, with the mass of genuine subhaloes being added to their parent halo. The table also shows the decomposition of the baryonic mass into gas and stars. We should note that the mass found in haloes depends on the resolution of a simulation, therefore Table 1 only gives the fraction of mass in haloes which can be resolved in the Illustris simulation. The resolution limit in terms of mass is

primarily given by the mass of a single dark matter particle which is $6.26 \times 10^6 M_\odot$. To detect gravitationally bound haloes, a minimum of about 30 particles are required. Thus, the threshold for halo detection in Illustris is approximately $2 \times 10^8 M_\odot$. A resolution study using a run with one-eighth of the mass resolution leads to similar results as the ones presented in Table 1. This suggests that the results are numerically robust. How much of the dark matter is expected to reside in haloes below the resolution limit also depends on the physical nature of the dark matter particle. Angulo & White (2010) find that for a 100 GeV neutralino dark matter particle only 5–10 % of the dark matter should not be part of a clump at redshift zero, and that the most abundant haloes have masses around $10^{-6} M_\odot$.

We find that about half of the total dark matter mass in the simulation volume is contained within haloes, while only 21 % of the baryonic mass resides within haloes. This evidently means that in the Illustris simulation, the mass ratio between baryons and dark matter is on average lower in haloes than the primordial mixture, $\Omega_b/\Omega_{\text{dm}}$. The latter would be the expected value if baryons traced dark matter perfectly. The second row of Table 1 shows that nearly all the halo baryons are in haloes with a total mass higher than $5 \times 10^9 M_\odot$. Less massive haloes in Illustris consist mainly of dark matter and are hence truly dark. We should note though that a $10^9 M_\odot$ halo is made up of only 160 dark matter particles, and the results will be less accurate at this scale than for haloes with higher numbers of particles (Vogelsberger et al. (2014a), see Trenti et al. (2010) for a discussion of the influence of particle number on the quality of halo properties). For haloes more massive than $5 \times 10^9 M_\odot$, we again see that the baryon/dark matter ratio is only half of the primordial ratio, and in the mass range between 10^{12} and $10^{13} M_\odot$, it drops to about one-third. Towards the most massive haloes of cluster size, this rises again to about 50 % and beyond of the expected primordial value.

Comparing these mass fractions bound in haloes with the results of the non-radiative run of the Illustris initial conditions, we find that the amount of dark matter in haloes is very similar. However, in the non-radiative run, the fraction of baryons in haloes is much higher and reaches about 40 %, which is roughly double the value of the full physics run. As the overall dark matter structure is very similar for the full physics and the non-radiative run, the difference in baryonic mass is a consequence of the feedback processes included in the full physics simulation (see also Sections 3.2 and 4).

The mass fraction in haloes also depends on the definition of halo mass. The values presented in Table 1 are the total gravitationally bound masses. Another common way to define the mass of haloes is to count the mass inside a sphere whose radius is set so that the mean enclosed density equals a reference density. If we measure the mass around the primary haloes of the SUBFIND friend-of-friend groups, and use as a reference density $200 \times \rho_{\text{mean}}$ (where ρ_{mean} denotes the mean matter density of the Universe) we find a total mass fraction of 48.1 % in haloes. Using the higher reference density $500 \times \rho_{\text{crit}}$ this value reduces to 26 %. We also want to note that for high-mass haloes, it makes a difference if the mass includes the contribution of subhaloes or not. In Illustris, 19.2 % of the haloes are subhaloes. They make up for 13.7 % of the total mass and 29.7 % of the stellar mass. Thus, if we neglected the contribution of sub-

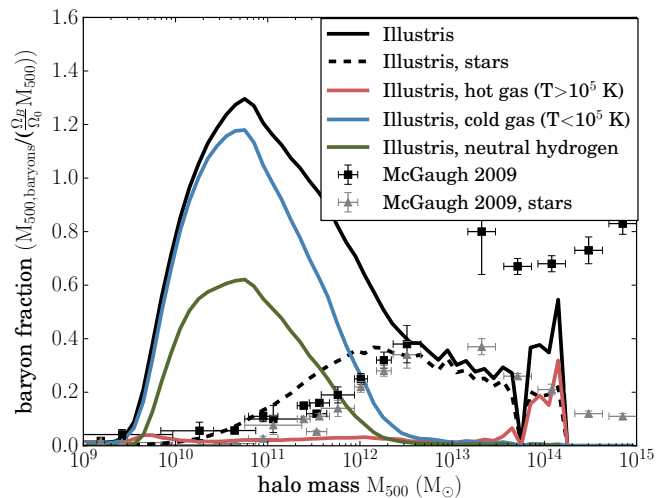


Figure 1. Baryon to total matter ratio inside central haloes of the Illustris simulation divided by the primordial ratio Ω_b/Ω_0 (solid black line). The x-axis gives the total mass of haloes inside a sphere with a mean density of 500 times the critical density. The dashed black line shows the contribution of stars, the red line the contribution of gas warmer than 10^5 K, the blue line gas colder than 10^5 K and the green line the amount of neutral hydrogen. The black squares and grey triangles represent observational data, taken from table 2 of McGaugh et al. (2010).

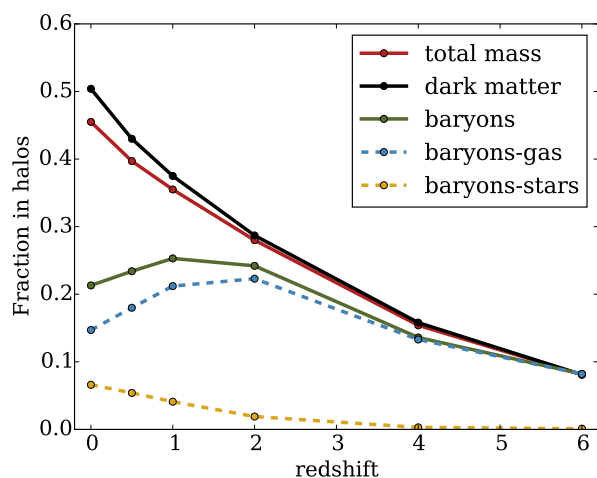


Figure 2. Redshift evolution of the mass inside haloes. The values for dark matter and baryons are normalized to the total dark matter and baryon mass in the simulation volume, respectively. The dashed lines show the contribution of gas and stars to the baryon fraction.

haloes, the haloes with a mass higher than $10^{14} M_\odot$ would be found to host only 4.4 % of the total matter, 4.9 % of the dark matter and 1.9 % of the baryons.

We further illustrate the baryon-to-dark matter ratio in Fig. 1, where we plot the ratio of the baryon content $M_{\text{baryon}}/M_{\text{total}}$ to the primordial baryon fraction Ω_b/Ω_0 against the halo mass. The baryon fraction is broken down into components of cold gas, hot gas, neutral hydrogen and stars, and the plot includes observational data compiled by McGaugh et al. (2010) for comparison. Only central haloes

Table 1. Mass fraction of dark matter and baryons inside haloes at $z = 0$. The mass fractions are given with respect to the total mass inside the simulation volume. The first row shows the fractions for all haloes in the Illustris full physics simulation. The second row gives the mass contribution of haloes with a total mass higher than $5 \times 10^9 M_\odot$ and the third and fourth rows show the respective values for haloes more massive than 10^{12} and $10^{13} M_\odot$, respectively. The last row gives the mass fraction for all haloes of the non-radiative Illustris run (no star formation, feedback or cooling).

	% of total	% of total baryonic mass			% of total
	dark matter mass	baryons	gas	stars	mass
all haloes	50.4 %	21.3 %	14.7 %	6.6 %	45.5 %
$M_{\text{tot}} > 5 \times 10^9 M_\odot$	44.6 %	21.3 %	14.7 %	6.6 %	40.7 %
$M_{\text{tot}} > 10^{12} M_\odot$	29.3 %	9.8 %	4.8 %	5.0 %	26.0 %
$M_{\text{tot}} > 10^{13} M_\odot$	20.1 %	7.2 %	4.0 %	3.2 %	18.0 %
$M_{\text{tot}} > 10^{14} M_\odot$	11.8 %	6.0 %	3.7 %	2.3 %	10.8 %
all haloes, non-radiative run	49.8 %	39.1 %	-	-	48.0 %

(those which are not subhaloes) have been used for this plot and only the mass inside R_{500c} (the radius inside of which the mean density is 500 times the critical density) is taken into account. A resolution study using data from a run with one-eighth of the mass resolution produced results very similar to Fig. 1.

In the regime of galaxy clusters, X-ray observations find a baryon to dark matter ratio between 70 and 100 % of the primordial value (Vikhlinin et al. 2006). For cluster sized haloes, Illustris finds a ratio around 40–50 %, but only small clusters are present in the limited simulations volume. This disagreement with observations has already been noted (see Fig. 10 in Genel et al. 2014) and has been attributed to a too violent radio-mode AGN feedback model. The radio-mode feedback model is used when the black hole accretion rates are low. It is most effective at removing gas from the haloes in the mass range from $10^{12.5}$ to $10^{13.5} M_\odot$, as at lower halo masses, the black holes are less massive and at higher halo masses, the potential wells are deeper. The model and the used parameters result in too large mass outflows from group-sized haloes and poor clusters (see Section 4 for a more detailed discussion of the model). As a considerable amount of mass is within group-sized haloes and clusters, the results about the distribution of baryons, which we present in the following sections, will be affected by the mass outflows.

Between $10^{10} M_\odot$ and $10^{11} M_\odot$, the baryon fraction is close to the primordial value Ω_b/Ω_0 . In this mass regime, the radio-mode AGN feedback plays only minor role as the black holes are less massive. The applied supernova feedback model is removing gas from the star-forming phase through galactic winds. However, the velocity of these winds is lower than the escape velocity and thus the supernova feedback model does not remove gas from the haloes. We find that most of the baryons in this mass range are at relatively low temperatures, and a large fraction of the gas is in neutral hydrogen. We should note though, that Illustris does not simulate the effects of the stellar radiation field on the gas, and therefore we cannot predict the ionization state exactly. The baryon fraction we find is higher than the fraction of detected baryons in McGaugh et al. (2010). However, these observations should be thought of as lower limits. A large fraction of the baryonic content of galaxies is expected to reside within the circumgalactic medium, which is subject to large observational uncertainties and is depending on model assumptions. Recent studies (Tumlinson et al. 2013; Bor-doloi et al. 2014; Werk et al. 2014) suggest that galaxies can

have substantial amounts of cold gas in their circum-galactic medium. In particular, we note that the baryon fraction we find in Illustris is compatible with the allowed range determined by Werk et al. (2014) (see their Fig. 11). The high baryon fraction in this mass range might also be connected to the finding that the galaxy stellar mass function in Illustris is too high for low mass galaxies (Genel et al. 2014; Vogelsberger et al. 2014a). We also recall that AREPO leads to more cooling than SPH-based codes for the same physics implementation (Vogelsberger et al. 2012).

In Fig. 2, we show the redshift evolution of the fraction of total mass, dark matter and baryon mass bound inside haloes. We see that the total mass inside haloes is monotonically increasing with time, reaching 45.5 % at redshift $z = 0$. Between redshift $z = 2$ and 1, the mass gain for the baryonic halo component is less pronounced than for dark matter, and from redshift $z = 1$ to 0 the fraction of baryons inside haloes even decreases. The onset of this decrease coincides with the radio mode AGN feedback becoming important (see Sijacki et al. 2015, for the evolution of the black hole accretion rate in the Illustris simulation). The figure also shows that the dominant contribution to the baryonic halo budget is from gas at all redshift. While the fractional contribution of stars to the total baryon budget increases with time, it reaches only a final value of 6.6 % at redshift $z = 0$.

3.2 Mass distribution in different dark matter density environments

The formation of large-scale structure is dominated by dark matter. Therefore, in this section we analyse the mass distribution with respect to different dark matter density environments. We compute the dark matter density through mapping the Illustris data on to a $(1024)^3$ grid covering the whole simulation volume. In Fig. 3 (a) we show a plot of the dark matter density and in Fig. 3 (b) of the baryon density in a slice through the simulation at redshift zero. The slice has an extent corresponding to the full 106.5×106.5 Mpc, and a thickness of one cell (104 kpc). For both the dark matter and the baryon slice we use a logarithmic colourmap with a range of 4.5 dex. The colourmap boundaries for the baryons have been set an order of magnitude lower than for the dark matter.

We note that the baryons appear more extended than the dark matter distribution, especially around high dark matter density regions. It is interesting to compare this to

Fig. 4, where we show the corresponding baryon density of the non-radiative run. Clearly, in the absence of feedback, the baryons are tracing the dark matter well on large scales.

Comparing the baryon distributions at different redshifts (Figs. 5 and 3), one can see that the extended baryon distributions around high dark matter density areas are less prominent at $z = 0.5$ and virtually absent at $z = 2$. The diameter of these regions is also increasing from $z = 0.5$ to 0. We conclude that the extended gas shells originate in gas which has been expelled from their host haloes due to radio-mode feedback, which becomes active at low redshift. A rough estimate from the diameter of these shells at different redshifts suggests that their expansion speed is between 500 and 1000 comoving km s^{-1} .

3.2.1 Mass distribution according to dark matter density

In Fig. 6, we present the fraction of the baryons at a given baryon and dark matter density. We binned the data in baryon and dark matter density using 200×200 bins. The diagonal line gives $\Omega_b/\Omega_{\text{dm}} \times \rho_{\text{dm}}$, which is where the baryons would lie if they traced dark matter perfectly. The colourmap shows the contribution of a bin to the total baryon mass. We find that there is a significant fraction of mass at high dark matter and high baryon densities, which corresponds to gas in haloes. A large fraction of baryons is at intermediate dark matter densities around the primordial dark matter density $\Omega_{\text{dm}}\rho_{\text{crit}}$. However, there are also many baryons at the lowest dark matter densities, the region we labelled ‘voids’.

It is interesting to observe the differences between the full physics and the non-radiative runs in Fig. 7, which shows the distribution of mass according to the dark matter density. We binned the data in dark matter density and then measured the mass contribution of a bin to the total baryonic or dark matter mass in the simulation volume. We see that the dark matter distribution in (b) is very similar for the full physics and the non-radiative run. However, there are notable differences for the baryons. For the full physics simulation, there is less mass at higher dark matter densities and significantly more mass at the lowest dark matter densities. This again is due to the feedback processes present only in the full physics simulation, which expel matter from the haloes out into dark matter voids.

3.2.2 Dark matter density and the cosmic web

The primary constituents of the large-scale structure differ in their dark matter density. Therefore we can use the dark matter density itself as a rough proxy to split up the simulation volume into regions corresponding to haloes, filaments and voids. We thus define the categories haloes, filaments and voids by assigning to them a certain dark matter density range¹. By summing the grid cells which fall into the respective dark matter density ranges we can measure the mass and volume of those regions. We show the resulting mass and volume fraction and the density range used for this classification in Table 2. The spatial distribution of the

categories in Table 2 is shown in Fig. 8. We show the same slice as in Fig. 3, and use a white colour for those cells that belong to the corresponding category.

The ‘haloes’ are defined to have a dark matter density higher than $15\rho_{\text{crit}}$. This density threshold has been chosen so that the halo region contains approximately the same amount of dark matter as the haloes of the halo finder. Thus, by construction, we find 49 % of the dark matter in haloes. But also the amount of baryons, which corresponds to 23 %, is in good agreement with Table 1. The volume fraction of the haloes is 0.16 %. The chosen threshold is also consistent with the resolution of the grid on which we calculate the density and the mass resolution of Illustris: a halo of $2 \times 10^9 M_{\odot}$ would result in an overdensity of $15 \times \rho_{\text{crit}}$, if all of its mass falls into a single grid cell. According to the SUBFIND halo catalogue, haloes smaller than $2 \times 10^9 M_{\odot}$ still host 4.8 % of the dark matter. However, many of those haloes will be sub-haloes and thus contribute their mass to the halo category. If we define the halo category to have densities higher than $30\rho_{\text{crit}}$, we find that it hosts 41.7 % of the dark matter and 21.6 % of the baryons, and all of the stars. This density cut at $30\rho_{\text{crit}}$ corresponds to the mass of a $4.2 \times 10^9 M_{\odot}$ halo in one cell. If we compare this value with the second row in Table 1 ($M_{\text{tot}} > 5 \times 10^9 M_{\odot}$) we again find that the value obtained using the dark matter density method is consistent with the value of the SUBFIND halo catalogue. We want to emphasize that the threshold density for the haloes is depending on the resolution of the grid, as it is the average density in one grid cell, and not the physical density at the outskirts of haloes.

The ‘filaments’ region, which we defined to have dark matter densities between 0.06 to $15 \rho_{\text{crit}}$, hosts 44.5 % of the dark matter and 46.4 % of the baryons. Its volume makes up 21.6 % of the total simulation volume. The filaments span a large density range in our definition. At the higher density end of this definition, between 5 and $15 \rho_{\text{crit}}$, the mass is mainly in ring-like regions around the bigger haloes, and no filamentary structure is visible in this density regime. This circumhalo region hosts about 11.1 % of the dark matter and 3.3 % of the baryons. The density boundary to the voids is motivated by Fig. 6, as the large bulk of mass in the denser parts of the filaments extends down to this value. Also, inspecting Fig. 8, this density range seems to correspond to what one would visually label as filaments. However, a different density range could as well be justified.

The ‘voids’ (dark matter densities between 0 and $0.06 \rho_{\text{crit}}$) contain only 6.4 % of the dark matter but 30.4 % of the baryons. The volume of the voids makes up 78.2 % of the total simulation volume. In that respect it is worthwhile to examine Figs. 10 and 11, where we show the temperature and the metallicity of the gas. If we compare the temperature and metallicity maps with Fig. 3 and Fig. 8, we see that the majority of the baryons in voids is composed of warm to hot gas enriched by metals. Those baryons have most likely been ejected from the haloes through feedback. Because the ejected material has a higher temperature than the other baryons in voids, we can use the temperature to discriminate between baryons naturally residing in voids and baryons which have been transported there. We define an additional ‘ejected material’ region in Table 2 which is defined as having a temperature higher than $6 \times 10^4 \text{ K}$ in addition to the dark matter density cut. With 23.6 % of the total

¹ The dark matter densities we use in this analysis are average densities over a volume of $(104 \text{ kpc})^3$.

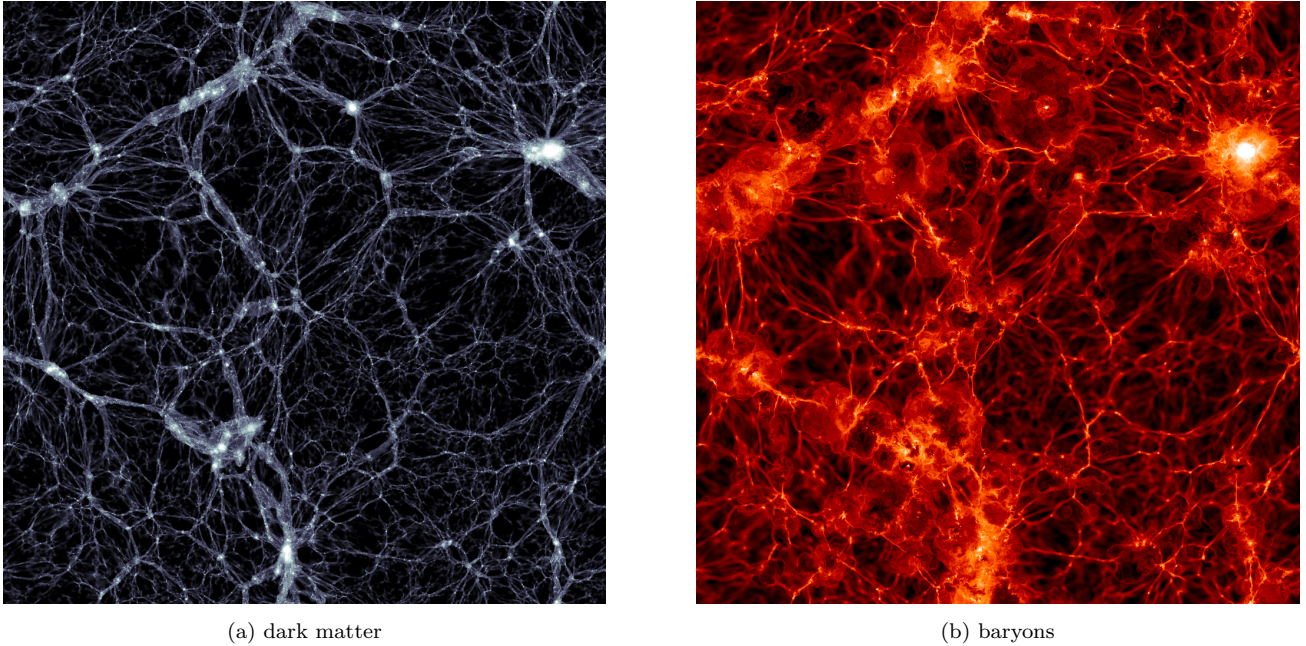


Figure 3. Dark matter and baryon density in a thin slice at $z = 0$. The slice covers the whole $(106.5 \text{ Mpc})^2$ extent of the simulation and has a thickness of 104 kpc (1 cell).

Table 2. Dark matter mass, baryonic mass and volume fraction in haloes, filaments and voids at $z=0$. The categories have been defined through dark matter density ranges. We also added a category ‘ejected material’ which corresponds to baryons inside the ‘voids’ region which have a temperature $T > 6 \times 10^4 \text{ K}$. The spatial regions to which these dark matter density regions correspond to are shown in Fig. 8.

component	dark matter density region (ρ_{crit})	% of total dark matter mass	% of total baryonic mass	% of total mass	% of total volume
haloes	> 15	49.2 %	23.2 %	44.9 %	0.16 %
filaments	0.06 - 15	44.5 %	46.4 %	44.8 %	21.6 %
voids	0 - 0.06	6.4 %	30.4 %	10.4 %	78.2 %
ejected material inside voids	0 - 0.06	2.6 %	23.6 %	6.1 %	30.4 %

baryons, this ‘ejected material’ region is responsible for most of the baryons in dark matter voids. In Fig. 9, the spatial region corresponding to the ejected material is plotted; note that it fills about 40 % of the voids. We should note though, that the ejected mass most likely heats some of the baryons already present in the voids. Therefore, we have probably overestimated the ejected mass in voids. However, through following the redshift evolution of the mass in voids we can give an estimate of the associate uncertainty, as we discuss below. We note that our findings for the volume fractions are generally in good agreement with simulations by [Cautun et al. \(2014\)](#).

3.2.3 Redshift evolution of matter and metals in haloes, filaments and voids

By applying the same dark matter density cuts at different redshifts, we can study the time evolution of the values reported in Table 2. This is done in Fig. 12, where we show how the baryons and dark matter divide into haloes, filaments and voids as a function of time. In Fig. 12 (a) we see that, starting at redshift $z = 2$, feedback begins to efficiently remove gas from haloes. At first, this only slows down halo

growth, but after a redshift of $z = 1$, it reduces the amount of baryons in haloes. In Fig. 12 (b) we see that the dark matter haloes, unaffected by feedback, continue to grow at the expense of the filaments. At high redshifts, the dark matter was distributed homogeneously with a density of $\Omega_{\text{dm}}\rho_{\text{crit}}$, and thus falls into the ‘filament’ category. The underdense regions of the voids were only created as matter from less dense regions was pulled into denser regions. Thus the fraction of dark matter in voids is increasing from $z = 6$ to 2. After $z = 2$, the amount of dark matter in voids is slowly decreasing due to accretion on to filaments. The baryons show a similar behaviour from $z = 6$ to 2. However, starting at a redshift of $z = 2$ ejected material is also transported into the voids, thus increasing their baryonic content. We see in Fig. 12 (a) that the mass increase of the ‘ejected material’ is higher than the mass increase of the ‘voids’. The most likely explanation is that the ejected mass heats gas already present in the voids, which means that we overestimate the mass of the ejected material with our density and temperature cut. If we assume that in the absence of feedback the baryons would show the same relative decrease from $z = 2$ to 0 as the dark matter, we would need to correct the value of the ejected material down to 20 %.

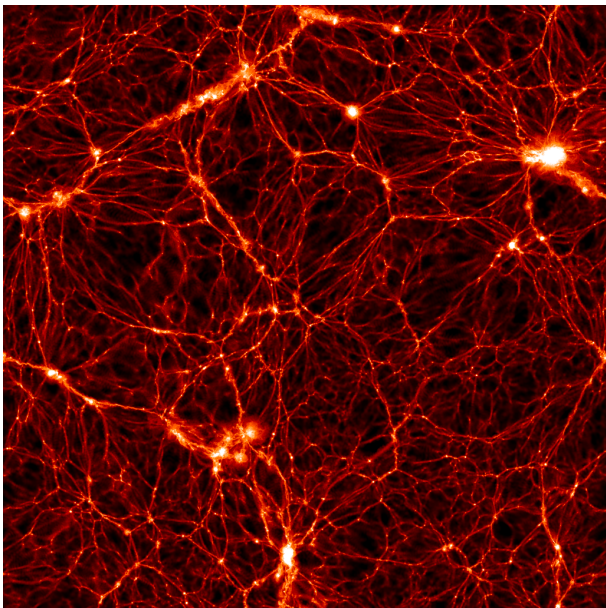


Figure 4. Baryon density of the non-radiative simulation (no star formation, feedback or cooling) at $z = 0$. The same slice as in Fig. 3 is displayed.

Illustris can also be used to probe the metal content in gas and stars. Star particles are stochastically formed when gas reaches densities above a threshold value ρ_{sfr} . A star particle is modelled as a single-age stellar population, for which the mass and metal return will be computed at every time-step. This material is then distributed over neighbouring gas cells (see Section 2.2 and 2.3 in Vogelsberger et al. 2013). In Fig. 13, we show the evolution of the metals in gas and stars normalized to the total metal mass at $z = 0$. Additionally, the figure shows which fraction of the metals in gas is residing in haloes, filaments or voids. We find that at $z = 0$, 36 % of the metals are locked up in stars and 64 % of the metals are in gas. Considering only the gaseous component, half the metals are within haloes and 28 % reside in the filaments. The remaining 22 % are located in voids. The average metallicity of the stars is 1.49 solar metallicities at $z = 0$, while the halo gas has about 0.37 solar metallicities on average. The average metallicity in filaments and voids is roughly 0.1 times the solar value.

3.3 Baryonic temperature–density relation

An alternative way to look at the distribution of baryons is to analyse them according to their density and temperature. This is more directly relevant to observations, as density and temperature are the important variables for emission and absorption mechanisms. In Fig. 14, we show the contribution of gas to the total baryonic mass in a temperature versus baryon density histogram. For this plot we directly use the Voronoi cell densities of the gas instead of the averaged densities we used in Section 3.2. We divide the baryons according to the same classification as has been used in Davé et al. (2001): diffuse gas having $\rho < 1000\rho_{\text{crit}}\Omega_b$ and $T < 10^5$ K, condensed gas with $\rho > 1000\rho_{\text{crit}}\Omega_b$ and $T < 10^5$ K, warm-hot gas with temperatures in the range $10^5 < T < 10^7$ K

and hot gas with temperatures above 10^7 K. We refer to the warm-hot gas also as WHIM.

We find that 21.6 % of the baryons are in the form of diffuse gas, located mainly in the intergalactic medium. The tight relation between temperature and density is due to the interplay of cooling through adiabatic expansion and photoionization heating (see also the discussion in Section 3.3 of Vogelsberger et al., 2012). The condensed gas amounts to 11.2 %. Most of the condensed gas is in a horizontal stripe around 10^4 K. As photoionization heating becomes less dominant but cooling time-scales shorten at higher densities, gas cools effectively down to this temperature. Since there is no metal and molecular line cooling, 10^4 K represents an effective cooling floor for the gas in this phase. The upward rising slope which extends from the ‘condensed’ region into the ‘WHIM’ region is due to an effective equation of state used for gas exceeding the density threshold for star formation (Springel & Hernquist 2003). The warm-hot medium makes up for 53.9 % of the baryons, while 6.5 % of the baryons are in hot gas.

The mass in these two categories corresponds to warm-hot shock-heated gas in haloes and filaments and material which has been ejected due to feedback from haloes (inspection of Fig. 10 shows that the ejected material is in the temperature range defining the WHIM region). If all the 23.6 % of the ejected material (see Table 2) had remained in haloes, this would have changed the warm-hot mass fraction to 30 % and increased the condensed fraction to 34.8 % (plus 6.6 % in stars).

The redshift evolution of the gas phases is given in Fig. 15, where we see that at high redshift, most of the gas has been in the form of a rather cold and diffuse medium. Starting at a redshift of $z = 4$, and more pronounced after redshift $z = 2$, the WHIM phase is gaining more and more mass, and by redshift zero, ends up containing most of the baryons.

4 DISCUSSION

Comparing the values of Table 1 with Table 2, we see a very good agreement at $z = 0$ between the SUBFIND halo catalogue and the haloes defined by a dark matter density cut. This suggests that our method of measuring the mass using the average dark matter density in a cell of our grid works reasonably well. However, we see deviations of 5–7 % for the mass in haloes at redshifts higher than 1. The reason for these deviations is that at higher redshifts the haloes are less massive, and thus some fall below the resolution limit of our grid.

Using the temperature-baryon density classification in Section 3.3, we find that 53.9 % of the baryons reside in the WHIM region. This is higher than the 30–40 % found in the work of Davé et al. (2001), or the work of Cen & Ostriker (2006), who reported between 40 and 50 % in the WHIM phase. This discrepancy is most likely due to the use of different feedback models. The importance of the feedback model is further underlined by the differences between the full physics and the non-radiative runs, which produce a nearly identical dark matter distribution but very different baryon distributions (see Fig. 7). In the full physics run only half the baryons are within haloes compared to the non-

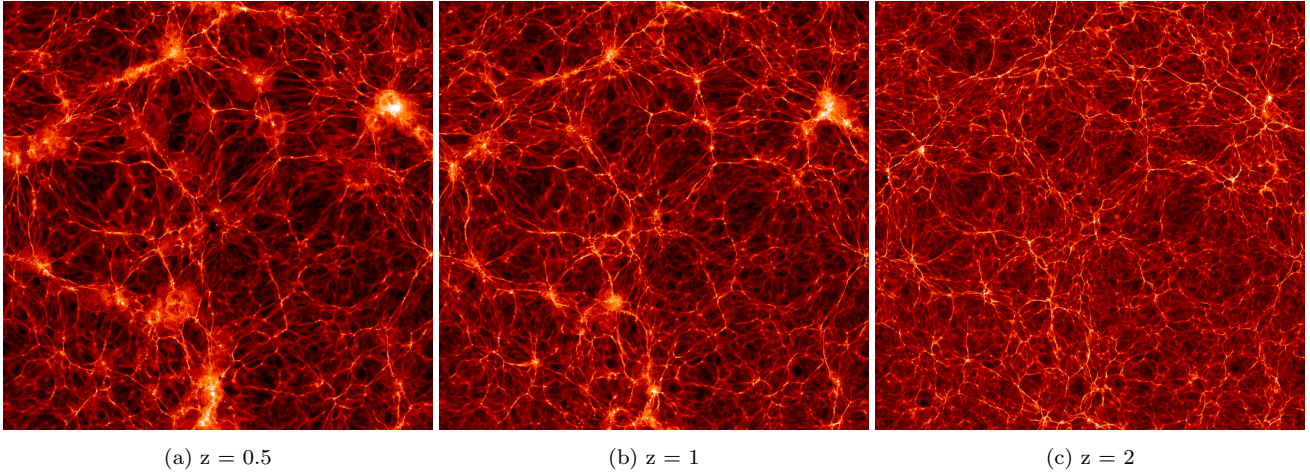


Figure 5. Redshift evolution of the baryon density. The same slice as in Fig. 3 has been used.

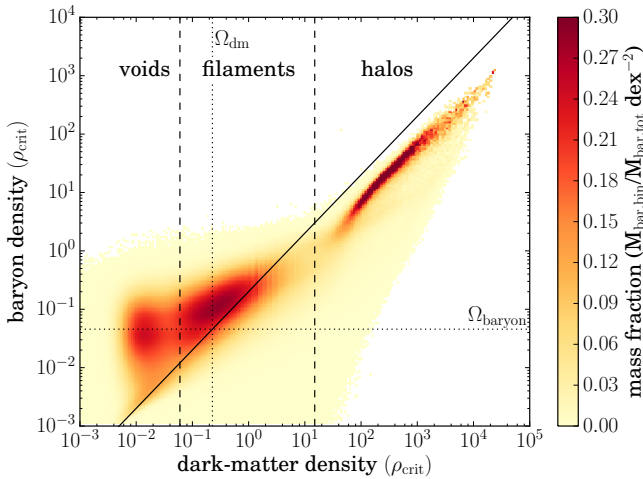


Figure 6. Histogram of the contribution of different dark matter and baryon density regions to the total baryonic mass. The dashed vertical lines indicate the boundaries of the dark matter density regions we defined in Section 3.2.1 to measure the mass in filaments, voids and haloes. The diagonal line indicates where a primordial mix of baryons and dark matter would lie.

radiative simulation (see Table 1). This difference is even more significant when we consider that the non-radiative run contains no radiative cooling and therefore the baryons cannot condense as easily into haloes as in the full physics run.

As stated in Section 3.2.1, it is interesting to note that we find 30 % of the baryons residing in voids. The reason for this is the strong radio-mode AGN feedback model, which is expelling baryonic matter from haloes and is responsible for nearly 80 % of the baryons ending up in voids. In a recent survey, Shull et al. (2012) find that 30 % of the baryons are missing in the low-redshift Universe. It would be tempting to explain these missing baryons with the baryons we find in voids. However, we have to be cautious in reaching this conclusion, as it is not clear whether the radio-mode feedback model implemented in Illustris is reliable. An indication that the feedback model of Illustris is too strong comes from the gas content of massive haloes. Observations of galaxy clus-

ter sized haloes find baryon fractions between 70 and 100 % of the primordial value (Vikhlinin et al. 2006). In contrast, we find (see Table 1) that the Illustris simulation produces a baryon fraction of only 50 % for haloes more massive than $10^{14} M_{\odot}$. The low gas content of massive haloes in the simulation has been attributed to the strong AGN radio-mode feedback (Genel et al. 2014). The radio mode is used when the accretion rate on to a black hole is low, and thus is strongest at low redshifts. Therefore, our results at low redshifts would most likely change if a weaker AGN feedback model was used.

Do the missing baryons in massive haloes explain the baryons we find in voids? The 149 haloes with a total mass higher than $10^{13} M_{\odot}$ contain 20.1 % of the total dark matter but only 7.2 % of the baryonic mass. Thus, 13 % of the total baryons are missing in these haloes. It therefore seems that the missing mass cannot explain the full 24 % of ejected material in voids. However, it is possible that material which is pushed out from the haloes might remove gas from the filaments. We should also note that the 24 % we quote is only the ejected mass inside voids. The actually ejected mass might be higher as some of the ejected material would still be in the filaments.

Other simulations of structure formation which include AGN feedback have produced baryon fractions in massive haloes in agreement with observations [McCarthy et al. (2011), Le Brun et al. (2014), Schaye et al. (2014), Planelles et al. (2013) or Khandai et al. (2015)]. It is beyond the scope of this paper to give a detailed comparison of different approaches. However, as the AGN feedback has a large impact on our results, we want to highlight some differences in the models. Most current cosmological simulations, including Illustris, include AGN feedback through modifications and extensions of the approach introduced in Springel et al. (2005). There, black holes are seeded when the hosting halo passes a threshold mass ($5 \times 10^{10} h^{-1} M_{\odot}$ for Illustris), and then Eddington-limited Bondi–Hoyle accretion is assumed. As the actual accretion region cannot be resolved, and the medium there is usually a mixture of hot gas and cold clouds, the Bondi–Hoyle accretion is sometimes enhanced by a factor α , which is invoked to compensate for the lack of resolution. In Illustris, this accretion enhancement parameter is

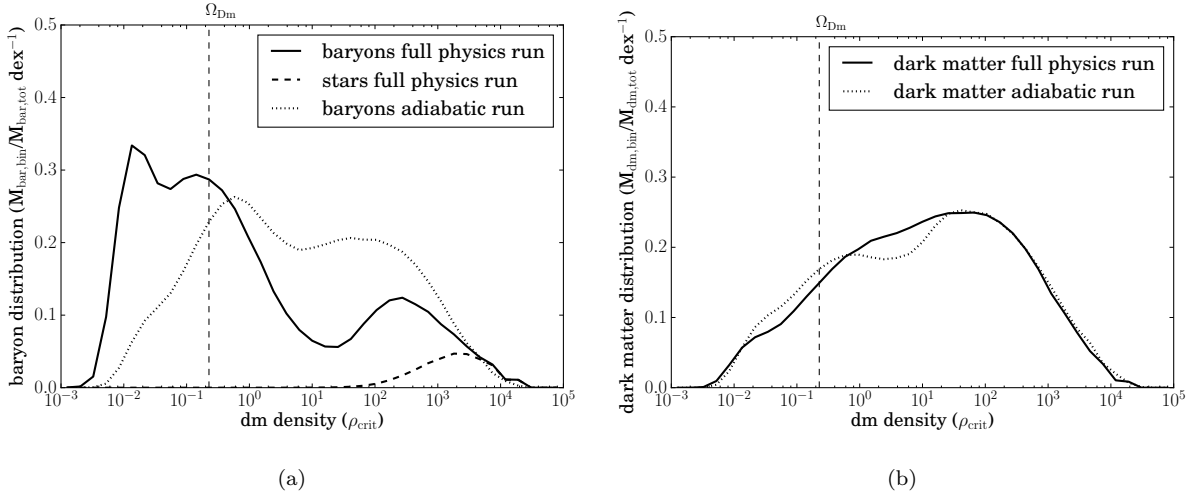


Figure 7. Baryon and dark matter mass distribution with respect to the dark matter density at $z = 0$. In (a), it is shown how much baryonic mass resides in an environment with a given dark matter density. The y -axis shows the fraction of baryonic mass in a dark matter density bin to the total baryonic mass in the simulation volume. The solid line represents the data from the full physics run and the dotted line shows the values for the non-radiative run. The dashed line gives the contribution of stars to the baryons in the full physics run. In (b), we show the analogous plot for the dark matter mass.

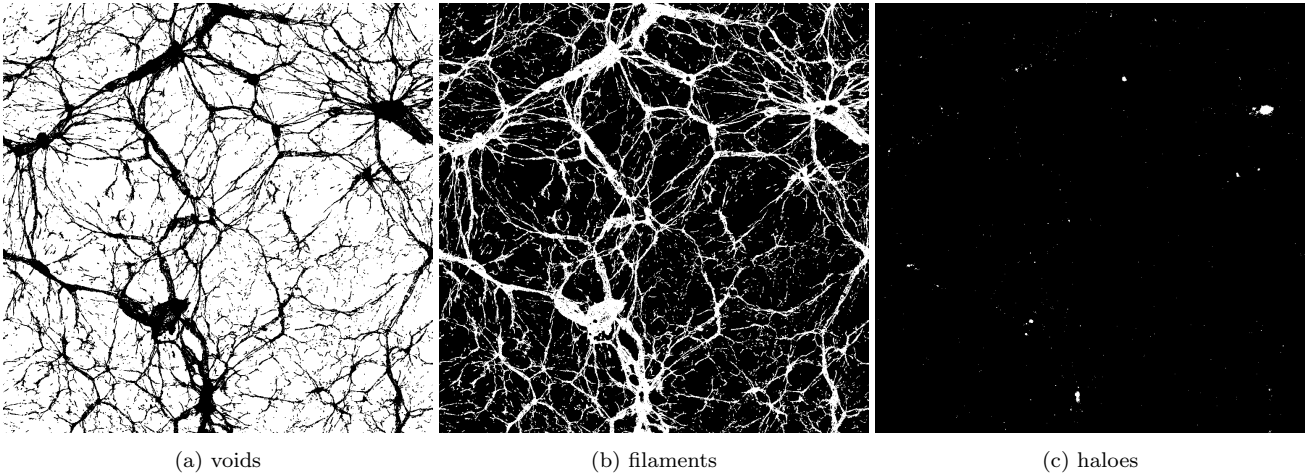


Figure 8. Spatial regions corresponding to the dark matter density ranges defined in Table 2. If a cell's dark matter density is inside the corresponding region it is drawn in white, otherwise it is black. The same slice as in Fig. 3 has been used.

set to $\alpha = 100$. It is further assumed that a fraction ϵ_r (set to 0.2 in Illustris) of the rest mass energy of the accreted mass is converted into energy, and a fraction of this energy in turn couples to the surrounding material. In Illustris, a modification of the model by Sijacki et al. (2007) is used, where a distinction between a quasar mode and a radio mode has been introduced. The quasar mode is assumed to be active if the accretion rate is above 5 % of the Eddington rate, and the radio mode, is used below this threshold. In the quasar mode, a fraction $\epsilon_f = 0.05$ of the AGN luminosity is coupled thermally to cells around the black hole. In the radio mode, the AGN is assumed to inject energy into bubbles, whose radius and distance to the black hole are computed according to Sijacki et al. (2007). The radio mode is assumed to have a higher coupling efficiency of $\epsilon_m = 0.35$. The radio mode bubbles are not formed continuously, but only after the mass of the black hole increased by a specified value δ_{BH} (15 % in Illustris). If the fractional mass increase $\Delta M/M$ surpasses

δ_{BH} , the energy $\epsilon_m \epsilon_r \Delta M c^2$ is put into a bubble. Thus, δ_{BH} controls the frequency and energy of bubbles.

Among the recent hydrodynamical simulations of galaxy formation mentioned above, Illustris is the only simulation which makes a distinction between radio and quasar mode in this way. Planelles et al. (2013) also use different efficiencies for radio and quasar mode, but the energy is coupled to surrounding particles in the same way for both modes. The model of Booth & Schaye (2009), which is used in McCarthy et al. (2010), Le Brun et al. (2014) and Schaye et al. (2014) does not discern between radio and quasar mode. A further difference between Illustris and Booth & Schaye (2009) is that they use a different accretion model. Instead of a constant value for the accretion enhancement, α is set to 1 at low gas densities and varies as a power law of density at higher densities (see Booth & Schaye 2009, for a discussion). In addition to this, Schaye et al. (2014) include a model which can lower the accretion rate in order

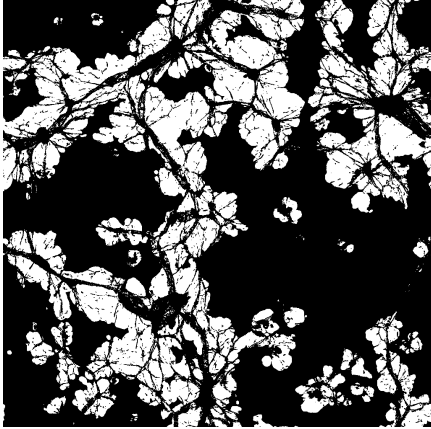


Figure 9. Spatial region corresponding to the ‘ejected baryons’ range of Table 2. In addition to the dark matter density cut, we here require a temperature higher than $T > 6 \times 10^4 \text{K}$.

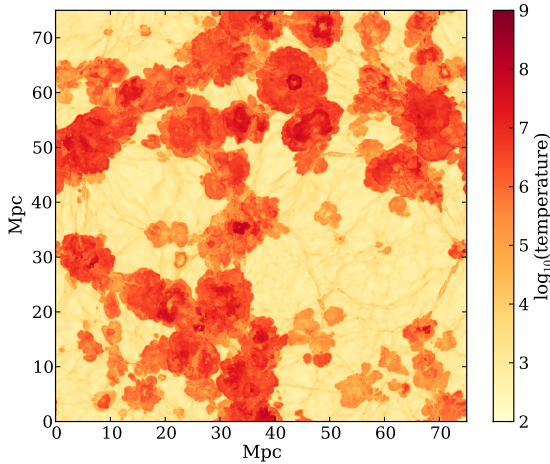


Figure 10. Temperature field of the gas in the slice of Fig. 3. We see that the gas forms hot bubbles around the haloes and filaments.

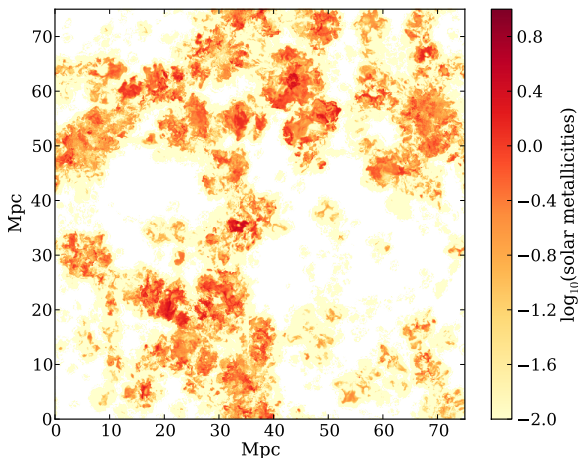


Figure 11. Plot of the gas metallicity for the slice which has been used in Fig. 3. The extended baryon distributions which protrude into the dark matter voids are rich in metals, suggesting that feedback processes are the cause of the extended distribution.

to account for the angular momentum of accreting gas (see Rosas-Guevara et al. 2015). Also, they use a radiation efficiency of $\epsilon_r = 0.1$ and a coupling efficiency of $\epsilon_f = 0.15$. In order to prevent that the injected energy is cooled away immediately, the feedback energy is not emitted continuously, but only once enough energy has accumulated to lead to a heating ΔT of 10^8K . The energy is then injected into one particle close to the black hole (or multiple particles if the energy produced per time-step is high enough to heat several particles to 10^8K).

There are also differences with respect to the used hydrodynamical scheme. Vogelsberger et al. (2012) found that the SPH code GADGET3 produces higher temperatures in haloes than the moving-mesh code AREPO, which has been employed in Illustris. They argue that this higher temperature has to do with spurious dissipation in SPH related to the higher numerical noise in this method. This might partly explain why the AGN feedback efficiency parameters had to be set higher in Illustris than in a comparable SPH simulation in order to reach the same suppression of star formation in massive haloes. Also, the mass resolution in McCarthy et al. (2010) and Le Brun et al. (2014) is very low compared to Illustris, which could lead to different density estimates at the black hole and thus influence the accretion rates significantly, even if the same accretion model was used.

For lower mass haloes AGN feedback is less important, as lower mass haloes typically have less massive black holes and the AGN luminosity scales with the square of black hole mass. Therefore, at low to medium masses the dominant feedback process regulating star formation is stellar feedback. A part of the stellar feedback is already implicitly included through the effective equation of state for star forming gas (Springel & Hernquist 2003). In addition to this, Illustris uses a non-local ‘wind’ feedback scheme (see Vogelsberger et al. (2013)), where a part of the star forming gas can be stochastically converted into wind particles. These wind particles are allowed to travel freely for some time (or until a density threshold is reached) before their mass and energy is deposited into the appropriate gas cell. Without these feedback processes, galaxies would form too many stars (the so called over-cooling problem). Thus the parameters of this models will also influence the results we presented (especially the region below $10^{12} M_\odot$ in Fig. 1). The Illustris stellar mass function is a bit too high in this mass range, suggesting that the feedback should be more effective in preventing star formation. Similarly, we find a high baryon fraction around unity in these haloes. As stated in Section 3, there are substantial observational uncertainties for the baryon fraction in this mass range, and the observations we included in Fig. 1 are to be thought of as lower limits.

We should caution however that while the feedback of Illustris is so strong that it depletes the massive haloes of their gas, the stellar mass function of Illustris is still too high for haloes with a stellar mass above $10^{12} M_\odot$ (see Fig. 3 in Genel et al. 2014). This indicates that the feedback is not efficient enough in suppressing star formation at this mass scale. Simply tuning the energy parameters of the feedback model cannot resolve the tension between the low gas content in massive haloes on one hand and the too high stellar mass function on the other hand. Either the AGN feedback model has to be modified (Genel et al. 2014, suggests making

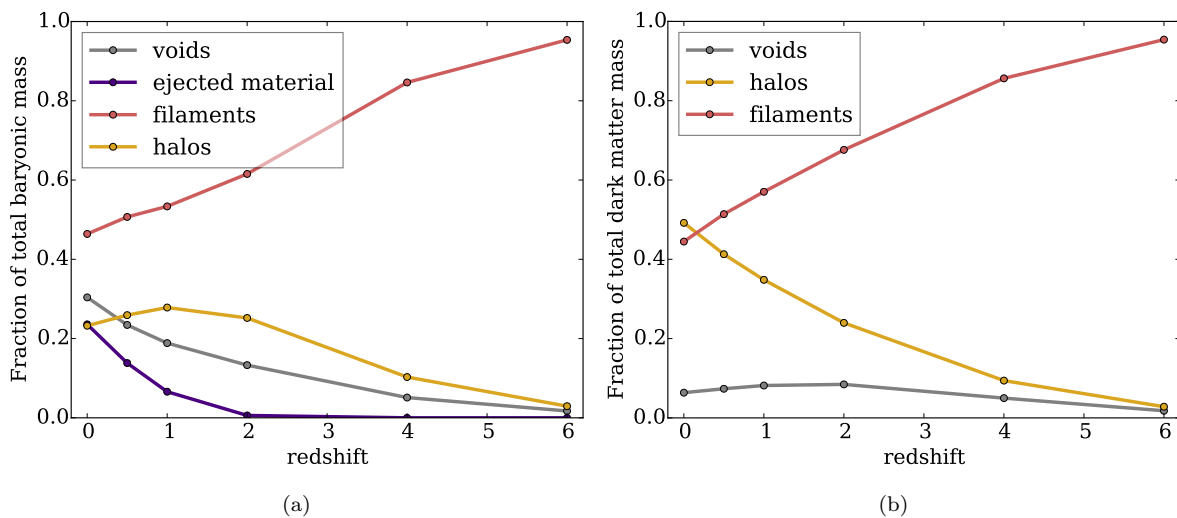


Figure 12. Redshift evolution of the contribution of haloes, voids and filaments to the total baryonic mass (a) and the total dark matter mass (b). While the evolution of the baryons and the dark matter is similar at redshifts higher than two, at low redshifts the haloes, lose baryons due to feedback processes while the dark matter in haloes is still growing.

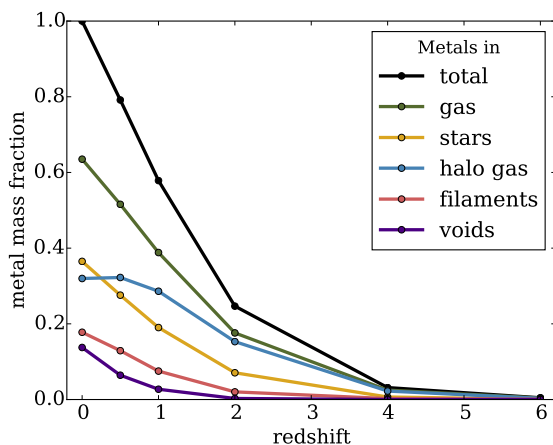


Figure 13. Evolution of metal fractions in gas and stars. The values are normalized to the total metals at $z = 0$, and the contribution of haloes, filaments and voids to the metals budget in gas is shown.

the duty cycle longer and thus avoiding short strong bursts) or this is a hint that other, so far neglected processes are important. It will be interesting to see if improved feedback models, which reproduce the baryon fraction in massive haloes correctly, will continue to find such a significant amount of baryons in dark matter voids.

5 SUMMARY

We investigated the global mass distribution of baryons and dark matter in different structural components of the Illustris simulation. By attributing dark matter density regions to the constituents of the cosmic web, we could measure the mass and volume of haloes, filaments and voids, as summarized in Table 2.

At redshift $z = 0$ we find that the haloes host 44.9 % of the total mass, 49.2 % of the dark matter and 23.2 % of

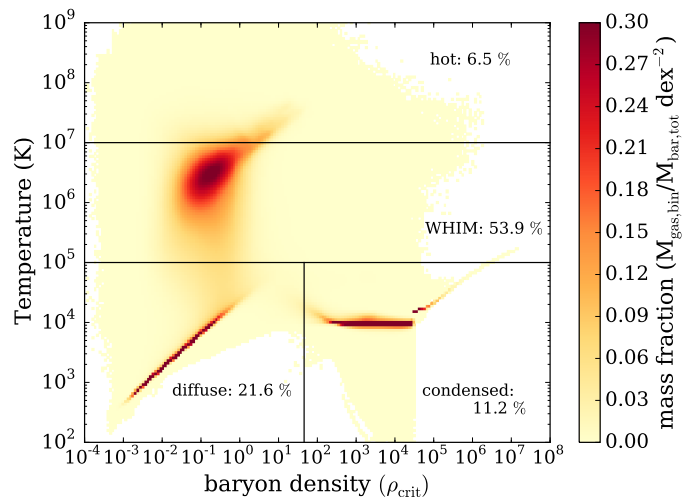


Figure 14. Mass fraction of gas to total baryons in temperature versus baryon density space. We subdivide the histogram into hot gas, diffuse gas, condensed gas and warm-hot intergalactic medium (WHIM). The mass fractions in these regions at $z = 0$ are indicated in the figure.

the baryons. Their volume fraction amounts to only 0.16 % of the total simulation volume. The filaments host 44.5 % of the dark matter and 46.4 % of the baryons and correspond to 21.6 % of the simulation volume. The dark matter voids contain 6.4 % of the dark matter but 30.4 % of the baryons, and the volume fraction of the voids amounts to 78.2 %. About 80 % of the baryons inside voids correspond to gas which has been ejected from haloes due to feedback processes. Most of this material, which occupies one third of the volume of the voids, has been ejected at redshifts lower than $z = 1$.

An analysis of a comparison run, in which star formation, cooling and feedback had been switched off, showed that the baryons trace dark matter well in a non-radiative

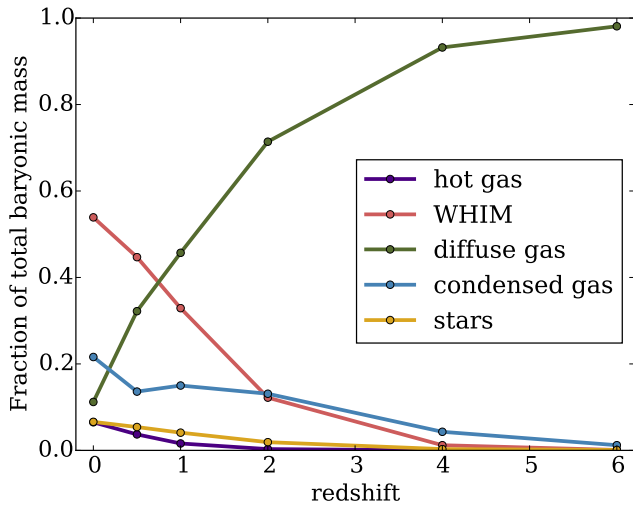


Figure 15. Redshift evolution of the mass fraction in the gas phases of Fig. 14. In addition to the gas phases, we also include the contribution of stars.

model, which is not the case for the full physics simulation. This demonstrates that the feedback model has significant consequences for the global mass distribution. While the feedback model of Illustris succeeds in reproducing a realistic stellar mass function, the low baryon fraction in massive haloes suggests that the feedback model is not correctly reproducing their gas content. At the moment it is still unclear whether our analysis would produce similar results with a different feedback model. Work on improved feedback models is ongoing, and it will be interesting to clarify this question in future studies based on a next generation of simulation models.

ACKNOWLEDGEMENTS

MH and DS thank their colleagues at the Institute for Astro- and Particle Physics at the University of Innsbruck for useful discussions, especially Francine Marleau, Dominic Clancy, Rebecca Habas and Matteo Bianconi. DS acknowledges the research grant from the office of the vice rector for research of the University of Innsbruck (project DB: 194272) and the doctoral school - Computational Interdisciplinary Modelling FWF DK-plus (W1227). This work was supported by the Austrian Federal Ministry of Science, Research and Economy as part of the UniInfrastrukturprogramm of the Focal Point Scientific Computing at the University of Innsbruck. SG acknowledges support provided by NASA through Hubble Fellowship grant HST-HF2-51341.001-A awarded by the STScI, which is operated by the Association of Universities for Research in Astronomy, Inc., for NASA, under contract NAS5-26555. VS acknowledges support through the European Research Council through ERC-StG grant EXAGAL-308037.

REFERENCES

Angulo R. E., White S. D. M., 2010, *MNRAS*, 401, 1796

- Bell E. F., McIntosh D. H., Katz N., Weinberg M. D., 2003, *ApJ*, 585, L117
- Booth C. M., Schaye J., 2009, *MNRAS*, 398, 53
- Bordoloi R. et al., 2014, *ApJ*, 796, 136
- Bregman J. N., 2007, *ARA&A*, 45, 221
- Cautun M., Van De Weygaert R., Jones B. J. T., Frenk C. S., 2014, *MNRAS*, 441, 2923
- Cen R., Ostriker J. P., 1999, *ApJ*, 514, 1
- Cen R., Ostriker J. P., 2006, *ApJ*, 650, 560
- Danforth C. W., Shull J. M., 2008, *ApJ*, 679, 194
- Davé R., Hernquist L., Katz N., Weinberg D. H., 1999, *ApJ*, 511, 521
- Davé R. et al., 2001, *ApJ*, 552, 473
- Fukugita M., Peebles P. J. E., 2004, *ApJ*, 616, 643
- Genel S. et al., 2014, *MNRAS*, 445, 175
- Gupta A., Mathur S., Krongold Y., Nicastro F., Galeazzi M., 2012, *ApJ*, 756, L8
- Kaasra J. et al., 2013, ([arXiv:1306.2324](https://arxiv.org/abs/1306.2324))
- Khandai N., Di Matteo T., Croft R., Wilkins S., Feng Y., Tucker E., DeGraf C., Liu M.-S., 2015, *MNRAS*, 450, 1349
- Kirkman D., Tytler D., Suzuki N., O’Meara J. M., Lubin D., 2003, *ApJS*, 149, 1
- Le Brun A. M. C., McCarthy I. G., Schaye J., Ponman T. J., 2014, *MNRAS*, 441, 1270
- McCarthy I. G. et al., 2010, *MNRAS*, 406, 822
- McCarthy I. G., Schaye J., Bower R. G., Ponman T. J., Booth C. M., Vecchia C. D., Springel V., 2011, *MNRAS*, 412, 1965
- McGaugh S. S., Schombert J. M., de Blok W. J. G., Zagursky M. J., 2010, *ApJ*, 708, L14
- Nelson D. et al., 2015, *Astron. Comput.*, 13, 12
- Nicastro F., Elvis M., Fiore F., Mathur S., 2005, *Adv. Space Res.*, 36, 721
- Nicastro F. et al., 2013, *ApJ*, 769, 90
- Planck Collaboration 2015, preprint, ([arXiv:1502.01589](https://arxiv.org/abs/1502.01589))
- Planelles S., Borgani S., Dolag K., Ettori S., Fabjan D., Murante G., Tornatore L., 2013, *MNRAS*, 431, 1487
- Rosas-Guevara Y. M. et al., 2015, *MNRAS*, 454, 1038
- Schaye J. et al., 2014, *MNRAS*, 446, 521
- Shull J. M., Smith B. D., Danforth C. W., 2012, *ApJ*, 759, 23
- Sijacki D., Springel V., Di Matteo T., Hernquist L., 2007, *MNRAS*, 380, 877
- Sijacki D., Vogelsberger M., Genel S., Springel V., Torrey P., Snyder G. F., Nelson D., Hernquist L., 2015, *MNRAS*, 452, 575
- Simionescu A. et al., 2011, *Science*, 331, 1576
- Smith B. D., Hallman E. J., Shull J. M., O’Shea B. W., 2010, *ApJ*, 731, 6
- Springel V., 2010, *MNRAS*, 401, 791
- Springel V., Hernquist L., 2003, *MNRAS*, 339, 289
- Springel V., White S., Tormen G., Kauffmann G., 2001, *MNRAS*, 328, 726
- Springel V., Di Matteo T., Hernquist L., 2005, *MNRAS*, 361, 776
- Torrey P., Vogelsberger M., Genel S., Sijacki D., Springel V., Hernquist L., 2014, *MNRAS*, 438, 1985
- Trenti M., Smith B. D., Hallman E. J., Skillman S. W., Shull J. M., 2010, *ApJ*, 711, 1198
- Tumlinson J. et al., 2013, *ApJ*, 777, 59
- Vikhlinin A., Kravtsov A., Forman W., Jones C., Markevitch M., Murray S. S., Van Speybroeck L., 2006, *ApJ*
- Vogelsberger M., Sijacki D., Keres D., Springel V., Hernquist L., 2012, *MNRAS*, 425, 3024
- Vogelsberger M., Genel S., Sijacki D., Torrey P., Springel V., Hernquist L., 2013, *MNRAS*, 436, 3031
- Vogelsberger M. et al., 2014a, *MNRAS*, 444, 1518
- Vogelsberger M. et al., 2014b, *Nature*, 509, 177
- Weinberg D. H., Miralda-Escude J., Hernquist L., Katz N., 1997, *ApJ*, 490, 564
- Werk J. K. et al., 2014, *ApJ*, 792, 8